



# Zn/Co-ZIF-Derived Composites as High-Performance Anode Materials for Sodium-Ion Batteries

Chonghua Shi<sup>1</sup> · Xinyu Liu<sup>1</sup> · Jing Wang<sup>1</sup> · Shaowei Yao<sup>1</sup>

Received: 30 August 2023 / Accepted: 12 January 2024 / Published online: 8 February 2024  
© The Minerals, Metals & Materials Society 2024

## Abstract

Composite materials derived from zeolite imidazolate frameworks (Zn/Co-ZIFs) have a unique porous structure, which has been used in the field of energy storage and catalysis. In this work, by direct heat treatment of Zn/Co-ZIFs, composite materials (Zn/Co-NPC (N-doped porous carbon) composites) of Zn and Co distributed uniformly in NPC were obtained. The pore structure and specific surface area of the composites were tuned by adjusting the heat-treatment temperature. Testing results show that the specific surface area and average pore size of the composites (at 700°C) are 272.3 m<sup>2</sup> g<sup>-1</sup> and 8.4 nm, respectively. When used as anode material for sodium-ion batteries, the composites have a high reversible specific capacity of 269.1 mAh g<sup>-1</sup> (100 mA g<sup>-1</sup> current density) after 100 cycles, and also have excellent rate capability. Therefore, this work provides new insights for the future synthesis of anode materials for sodium-ion batteries with unique structure and high capacity.

**Keywords** Zeolite imidazolate frameworks · composite materials · anode materials · sodium-ion battery

## Introduction

With the rapid development of the modern economy and science and technology, the commercialization of batteries has brought amazing changes to our lives. In the context of all kinds of electronic products that need batteries to provide energy, lithium-ion batteries have been widely used in electronic devices and energy storage systems due to their advantages of excellent energy density, long-term cycle stability, and low self-discharge rate. Unfortunately, as the demand for lithium resources continues to grow, so does its cost. Because of the low concentration of lithium in the ocean, large-scale extraction of lithium from seawater is difficult to achieve at the current stage. By contrast, sodium is not only more abundant in the Earth's crust, but it is also more abundant in the ocean and is easy to extract. As such, sodium has an absolute cost advantage over lithium. In addition, sodium and lithium are two elements in Group IA that are next to each other; sodium has lithium-like physical and

chemical properties, and the structure and working principle of sodium-ion batteries are basically the same as those of lithium-ion batteries. Therefore, sodium-ion batteries have become candidates to replace traditional lithium-ion batteries.<sup>1–3</sup> However, the radius of sodium ions is larger than that of lithium ions, which will cause large volume changes in the electrode material during the discharging and charging process, making the collapse of the electrode structure and amorphization more serious. Based on this background, the rapid and stable insertion/extraction of sodium ions during the charging and discharging process is a great challenge. Therefore, finding suitable electrode materials with high sodium storage capacity has become an important task.<sup>4,5</sup>

Although sodium-ion batteries and lithium-ion batteries have similar structures and operating principles, graphite—a successful practical anode material for lithium-ion batteries—has very low sodium storage capacity when used as anode material for a sodium-ion battery<sup>6</sup> (NaC<sub>70</sub>). Therefore, the development of new anode materials with novel structures and controllable composition is the only way to realize high-performance sodium-ion batteries. There are many ways to improve the electrochemical performance of anode materials for sodium-ion batteries. For example, hard carbon,<sup>7</sup> soft carbon,<sup>8</sup> and disordered carbon<sup>9</sup> have been used as anode materials. A hollow structure, mesoporous structure,

✉ Shaowei Yao  
yaoshaowei389@163.com

<sup>1</sup> College of Materials Science and Engineering, North China University of Science and Technology, Tangshan 063210, China

and sheet morphology of materials can also improve their electrochemical performance.<sup>10–12</sup> In addition, heteroatoms (such as N, P, S) are introduced into carbon-based materials to produce a variety of chemical configurations, including graphite N, pyridine N, and pyrrole N. Due to the introduction of heteroatoms, the physical and chemical properties of carbon-based materials, including conductivity, active site, and defect concentration, are much improved, thereby improving the electrochemical performance of sodium-ion batteries. Agrawal et al. introduced N atoms into nano-carbon spheres (NNCS) and micro-carbon spheres (NMCS), which were used as anode materials for sodium-ion batteries.<sup>13</sup> Raman spectra show that N-atom doping results in excellent electrochemical performance due to introducing structural defects. It has a reversible capacity of 243 mAh g<sup>-1</sup> at 30 mA g<sup>-1</sup> after 200 cycles.

Metal-organic frameworks (MOFs) are self-assembled by metal ions (such as Sn, Bi, Zn) and organic molecules, and MOFs exhibit a variety of structures including spherical, polyhedral, and sheet-like. Moreover, the material has attracted considerable attention from researchers in the field of energy storage because of its unique structure, open channel, and high specific surface area.<sup>14,15</sup> Zeolite imidazolate frameworks (ZIFs) are a common material in MOFs, which typically consist of transition metal Co/Zn ions and imidazole coordination to form a unique polyhedral structure. This unique structure not only inherits the porosity and adjustable pore size advantages of MOFs, but also has the high stability characteristics of the zeolite structure. When synthesized by different preparation methods and solvents, ZIFs have different morphology and porosity, so that they can play a role in a variety of fields. Additionally, ZIFs can be directly calcined as a precursor to obtain nanostructured composites. The composite material has good electrical conductivity, high specific surface area, and sufficient active sites, resulting in excellent electrochemical performance. At the same time, the composite has abundant nitrogen atom doping and high specific surface area, which provides sufficient space for insertion/extraction of sodium ions. In conclusion, ZIF-derived composites have high potential in the development of anode materials for sodium-ion batteries with high specific capacity, excellent rate performance, and long-term cyclic stability. Zheng et al.<sup>16</sup> reported N, P, F-doped hollow carbon nanocage composites (NPF-HCN) derived from ZIF-8, which have rich heteroatomic doping and a hollow porous structure. When used as anode material for sodium-ion batteries, the NPF-HCN electrode material achieved a reversible specific capacity of 220 mAh g<sup>-1</sup> at a current density of 5 A g<sup>-1</sup>. Kaneti et al. studied Ni-doped Co/CoO/N-doped composites derived from bimetallic ZIF as anode material for sodium-ion batteries.<sup>17</sup> At a current density of 500 mA g<sup>-1</sup>, the composite demonstrated specific capacity of 218 mAh g<sup>-1</sup> when used as a sodium-ion battery. The composites have many micropores and a high specific surface area (552 m<sup>2</sup> g<sup>-1</sup>). Based on these

advantages, better insertion/extraction of sodium ions can be promoted, thus improving the electrochemical performance of the anode. In previous studies, Zn/Co-ZIFs were obtained by a simple co-precipitation method. Zn/Co-ZIFs are directly heat-treated to obtain composites with a large specific surface area and suitable porous structure.

In this study, a simple design method is used to directly carbonize Zn/Co-ZIFs at different temperatures (600°C, 700°C, 800°C) to obtain porous carbon composites. The effect of pore structure on electrochemical performance is explored by microstructure and electrochemical performance tests. The obtained composites inherit the diamond dodecahedron structure of Zn/Co-ZIFs. When the heat treatment temperature is 700°C, the specific surface area of the composite is 272.3 m<sup>2</sup> g<sup>-1</sup> and the average pore diameter is 8.4 nm. As anode material for sodium-ion batteries, it has a highly reversible specific capacity of 269.1 mAh g<sup>-1</sup> for 100 cycles at 100 mA g<sup>-1</sup> current density. Due to the introduction of N atoms, the obtained composite has high sodium storage capacity. In addition, the suitable pore structure is conducive to sodium-ion insertion/extraction, thereby improving the rate performance and long-term cyclic stability of the composites. Therefore, ZIFs may be a promising candidate for sodium-ion storage of functional carbon. This also provides an opportunity and space for the rapid development of anode materials for sodium-ion batteries.

## Experimental Section

### Materials

Methanol (CH<sub>3</sub>OH, ≥ 99.9%) and absolute ethanol (99.5%) were purchased from Tianjin Yongda Chemical Reagent Co., Ltd. 2-Methylimidazole, cobalt nitrate hexahydrate, and zinc nitrate hexahydrate were obtained from Shanghai Aladdin Reagent Co., Ltd. Polyvinylpyrrolidone K30 (PVP) was obtained from Sinopharm Chemical Reagent Co., Ltd. All chemical reagents were used directly.

### Preparation of Zn/Co-NPC Composites

The synthesis of the Zn/Co-NPC (N-doped porous carbon) composites is shown in Fig. 1. A total of 2.97 g Zn (NO<sub>3</sub>)<sub>2</sub>·6H<sub>2</sub>O and 2.91 g Co (NO<sub>3</sub>)<sub>2</sub>·6H<sub>2</sub>O were dissolved in 300 mL methanol, then poured into 100 mL methanol solution mixed with 10 g 2-methylimidazole and 20 g PVP. The obtained mixed solution was magnetically stirred for 10 min, and then aged at room temperature for 24 h. The products after standing were washed several times with methanol and absolute ethanol in succession. After drying at 80°C, Zn/Co-ZIFs were obtained as a purple powder. Subsequently, Zn/Co-ZIFs were heated under N<sub>2</sub> atmosphere at heating

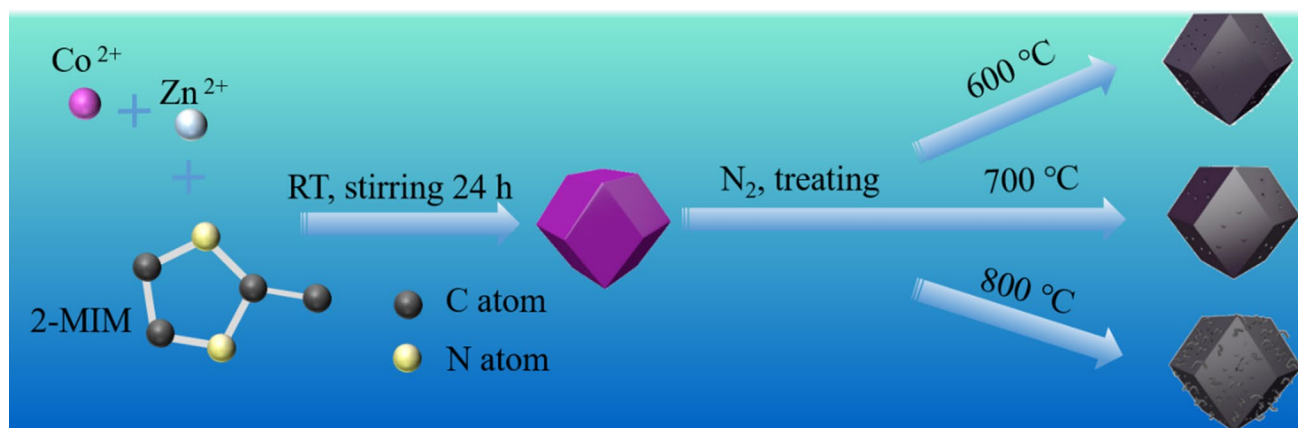


Fig. 1 Schematics of the synthesis process of Zn/Co-NPC composites.

temperatures of 600°C, 700°C, and 800°C, which yielded Zn/Co-NPC. Finally, black samples were obtained as Zn/Co-NPC composites, which were designated as Zn/Co-NPC600, Zn/Co-NPC700, and Zn/Co-NPC800 according to the different heat treatment temperatures.

### Material Characterization

The elemental composition and microstructure of the Zn/Co-NPC composites were observed by scanning electron microscopy (SEM, Hitachi S-3400-N), elemental mapping, and transmission electron microscopy (TEM, Hitachi H-800). The crystal phase of the Zn/Co-NPC composites was obtained by x-ray powder diffraction (XRD, D/Max 2500PC diffractometer) over a  $2\theta$  range of 10°–80°. The  $N_2$  adsorption-desorption curves of the Zn/Co-NPC composites were determined by the Barrett–Joyner–Halenda (BJH) and Brunauer–Emmett–Teller (BET) methods. Thermogravimetric analysis (TGA, NETZSCH STA 449C) was conducted in  $N_2$  and air atmosphere from 30°C to 800°C (heating rate of 10°C min<sup>-1</sup>). X-ray photoelectron spectroscopy (XPS, test condition: Mg-K $\alpha$  rays) was used to study the elemental composition and valence of the Zn/Co-NPC composites. Simultaneously, the binding energies of elements were corrected by using the C 1s peak in XPS data. The carbon skeleton structure of the Zn/Co-NPC composites was studied by Raman spectroscopy.

### Electrochemical Measurements

The prepared Zn/Co-NPC composites were used as the active materials and mixed with acetylene black and polyvinylidene fluoride (PVDF) in a weight ratio of 7:1.5:1.5 (in a dry environment). Afterwards, *N*-methyl-2-pyrrolidone (NMP) was added to prepare a uniform slurry, which was coated on copper foil. For electrochemical tests, the resulting

material was assembled in a glove box filled with argon for button battery assembly. The mass loading of the Zn/Co-NPC composites on the copper foil was about 1–1.5 mg cm<sup>2</sup>. The assembly sequence from front to back was as follows: anode electrode shell, pole piece, glass fiber diaphragm, sodium sheet, gasket, shrapnel, and cathode electrode shell. Finally, the assembly of the button battery was completed using a sealing machine. Glass fiber (Whatman) was used as the separator of the sodium-ion battery, and 1.0 M NaPF<sub>6</sub> (in DIGLYME = 100 vol.%) as the electrolyte. Galvanostatic discharge/charge experiments were carried out by a Land battery test system (CT2001A) over a voltage range of 0.01–3.0 V. Cyclic voltammetry (CV) and electrochemical impedance spectroscopy (EIS) were conducted on an electrochemical workstation (PGSTAT 204).

## Results and Discussion

### Structure and Morphology

The initial morphology and structural changes of the Zn/Co-ZIFs and obtained Zn/Co-NPC composites were observed through SEM images as shown in Fig. 2a, b, c, and d. The precursor Zn/Co-ZIFs show a regular rhomboidal dodecahedron structure. With the increase in heat treatment temperature, the uniform dodecahedron structure reveals obvious shrinkage and collapse, and even a small number of nanowires appear in the outer layer. When the temperature rises to 800°C, this phenomenon becomes increasingly pronounced. This is caused by the catalytic effect of Co and the thermal decomposition of organic precursors at high temperature.<sup>18</sup> The elemental mapping of Zn/Co-NPC700 is shown in Fig. 2e. It is found that C, N, Zn and Co are evenly distributed. In addition, Zn and Co are well dispersed in the carbon network.



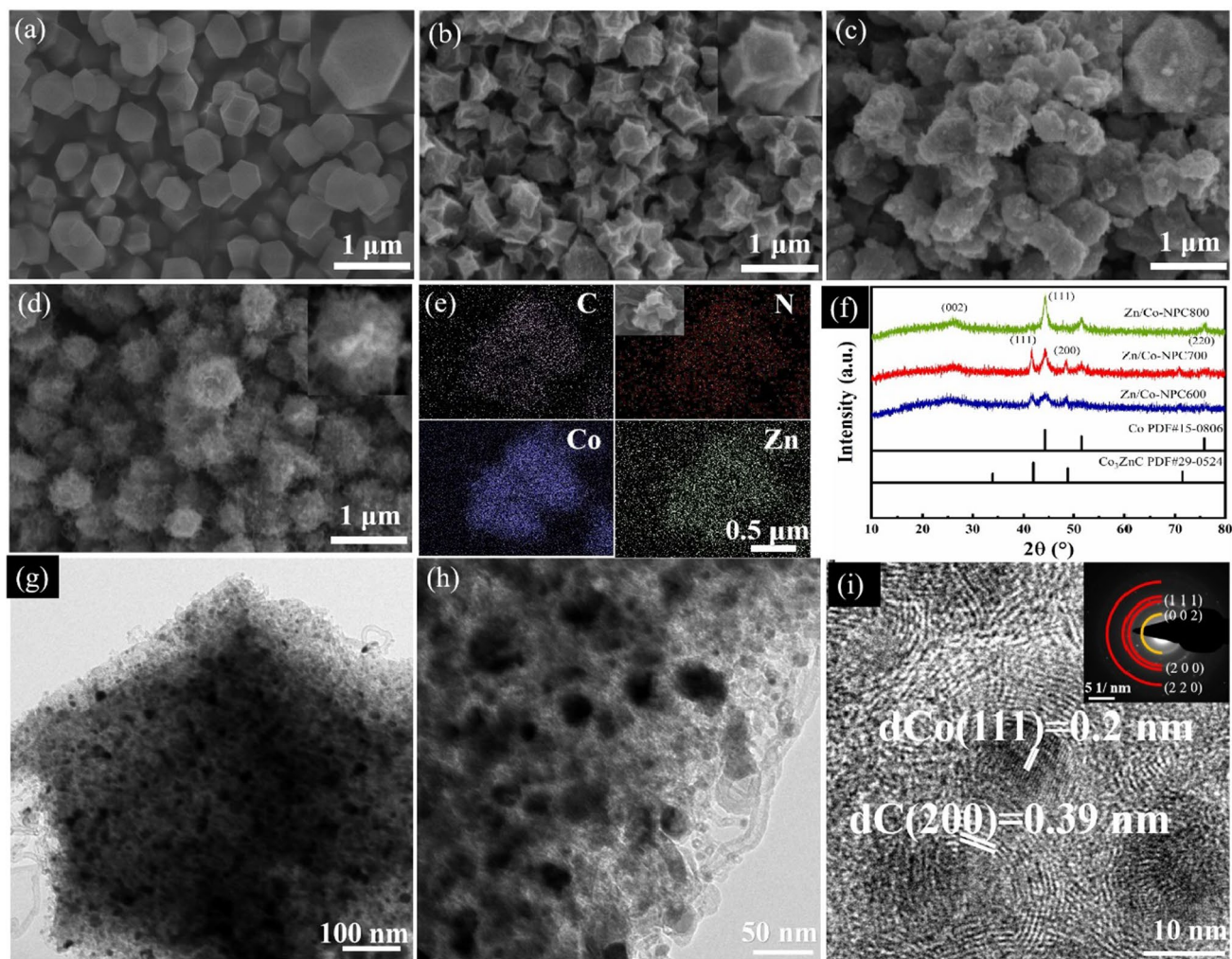


**Fig. 2** SEM images of (a) Zn/Co-ZIFs, (b) Zn/Co-NPC600, (c) Zn/Co-NPC700, and (d) Zn/Co-NPC800, and the upper right corner illustration shows enlarged images; (e) elemental mapping of Zn/Co-NPC700 and the SEM image of Zn/Co-NPC700 in the illustration; (f) x-ray diffraction patterns of Zn/Co-NPC composites; (g, h) TEM images, (i) high-resolution (HR)TEM images and (illustration of Fig. 2i) SAED of Zn/Co-NPC700.

In Fig. 2f, the XRD peaks of Zn/Co-NPC600, Zn/Co-NPC700, and Zn/Co-NPC800 at  $44^\circ$ ,  $51^\circ$ , and  $75^\circ$  correspond to the (111), (200), and (220) crystal planes of Co (JCPDS no. 15-0806), respectively. The wide peaks at about  $26^\circ$  correspond to the (002) crystal plane of C (JCPDS no. 89-8487). There is also a small amount of  $\text{Co}_3\text{ZnC}$  in Zn/Co-NPC600 and Zn/Co-NPC700 (JCPDS no. 29-0524).<sup>19</sup> TEM images of Zn/Co-NPC700 show that it is composed of small particles, the carbon skeleton, and epitaxial nanowires (Fig. 2g, h). The dodecahedral structure of Zn/Co-NPC700 shows obvious collapse and the appearance of nanowires in the outer layer, which is consistent with the above SEM images. In Fig. 2i, high-resolution (HR)TEM shows that the lattice fringe spacing of C, Co, and  $\text{Co}_3\text{ZnC}$  is 0.39 nm,

0.2 nm, and 0.22 nm, respectively. The rings of the selected area electron pattern (SAED) are well matched with the crystal planes of Co (111), (200), (220) and C (002), respectively, which is consistent with the XRD pattern above.

Figure 3a and b show the TGA curves of Zn/Co-ZIFs ( $30\text{--}800^\circ\text{C}$ ,  $\text{N}_2$ ) and Zn/Co-NPC700 ( $30\text{--}800^\circ\text{C}$ , air), respectively. The mass of the Zn/Co-ZIFs drops sharply from  $600^\circ\text{C}$  (27%), resulting in C–H bond breakage, and Zn is slowly consumed during the high-temperature carbonization process (Fig. 3a). In the air atmosphere, Zn/Co-NPC700 (Fig. 3b) has a serious mass loss of 52% at  $300\text{--}450^\circ\text{C}$ , which can be attributed to carbon loss and oxidation of Zn and Co.<sup>20</sup> At this time, Zn and Co content can be determined by Eqs. 1 and 2 as follows.

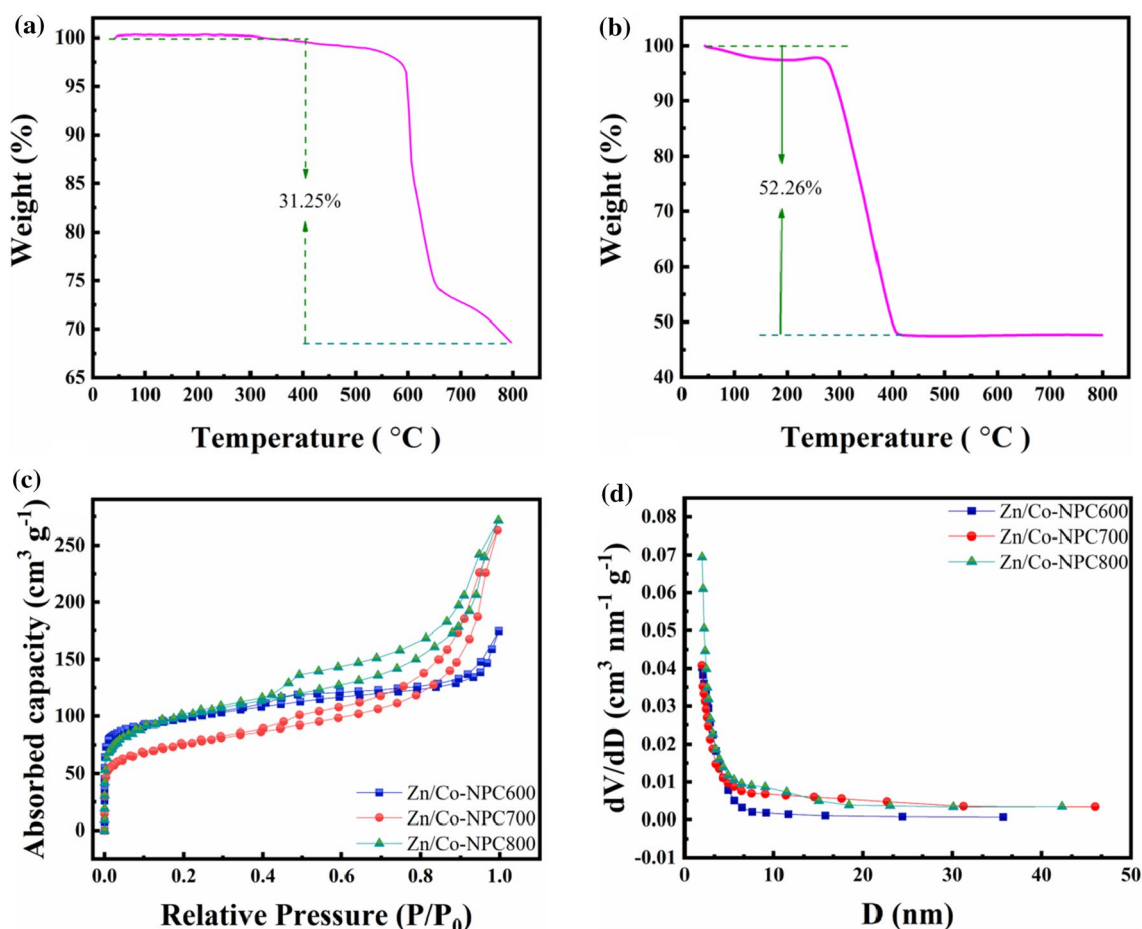


**Fig. 3** TGA curves of (a) Zn/Co-ZIFs in N<sub>2</sub> atmosphere and (b) Zn/Co-NPC700 in air atmosphere; (c) N<sub>2</sub> adsorption-desorption isotherms curves and (d) the corresponding pore-size distributions of Zn/Co-NPC composites.

$$\text{Co (wt. \%)} = 100 \times \frac{3 \times \text{molecular weight of Co}}{\text{molecular weight of Co}_3\text{O}_4 + \text{molecular weight of ZnO}} \times \frac{\text{final weight of Co}_3\text{O}_4 + \text{ZnO}}{\text{initial weight of Zn/Co - NPC}} \quad (1)$$

$$\text{Zn (wt. \%)} = 100 \times \frac{\text{molecular weight of Zn}}{\text{molecular weight of Co}_3\text{O}_4 + \text{molecular weight of ZnO}} \times \frac{\text{final weight of Co}_3\text{O}_4 + \text{ZnO}}{\text{initial weight of Zn/Co - NPC}} \quad (2)$$

Therefore, the content of Zn and Co is 9.7 wt.% and 26.4 wt.%, respectively.

Comparison of the EDS maps of the three groups of composites reveals that the atomic ratio of Zn:Co decreases with the increase in temperature (see supplementary Table S1). The results are in agreement with the above thermal analysis

results. The specific surface area and pore structure of Zn/Co-NPC composites were analyzed by N<sub>2</sub> adsorption/desorption isotherms, and the results show IV-type sorption isotherms (Fig. 3c, d). The BET specific surface area of Zn/Co-NPC600, Zn/Co-NPC700, and Zn/Co-NPC800 is 360.9 m<sup>2</sup> g<sup>-1</sup>, 272.3 m<sup>2</sup> g<sup>-1</sup>, and 363.3 m<sup>2</sup> g<sup>-1</sup>, respectively,

and the corresponding average pore sizes are 5.0 nm, 8.4 nm and 6.5 nm, respectively. Zn/Co-NPC800 shows a wide hysteresis loop, indicating that a large number of mesopores are produced. The pore size of the Zn/Co-NPC700 composite with an intermediate heat treatment temperature is mainly concentrated at 2–3 nm, and this composite has a smaller specific surface area. This is because, with the increase in calcination temperature, Zn with a lower boiling point (901 °C) will partially evaporate, which leads to a greater number of pores in the Zn/Co-NPC composites.<sup>21</sup> At higher calcination temperature, the rhomboidal dodecahedron structure collapses and the specific surface area decreases. The thermal catalytic effect of Co causes the outer layer of the polyhedron to produce nanowires, and the specific surface area increases accordingly,<sup>22,23</sup> which is consistent with the above SEM images. These results show that suitable surface area and pore structure are highly dependent on the calcination temperature of the material, and a suitable pore structure can improve the electrochemical performance of the material.

The elemental composition and chemical valence of Zn/Co-NPC700 were measured by XPS. The measurement results show the presence of C, N, Zn, and Co in Zn/Co-NPC700 (Fig. 4a, b, c, d, e), which is in good agreement with the above analysis of elemental mapping. In Fig. 4a, Zn/Co-NPC700 has three fitted component peaks in the N

1s spectra at 398.4 eV, 400.1 eV, and 401.3 eV, which can be assigned to pyridine, pyrrole, and graphitic nitrogen, respectively. This further confirms the presence of N in the composite, and its atomic percentage is about 11.3 at.%. Nitrogen doping can improve the conductivity and reactivity of Zn/Co-NPC700.<sup>24</sup> The peaks of the C 1s spectrum (Fig. 4b) at 284.7 eV, 285.9 eV, and 288.1 eV correspond to C=C, C=N, and C=O/C-N, respectively. The Co 2p spectrum can be fitted into two major peaks (Co2p<sub>3/2</sub> and Co2p<sub>1/2</sub>) and two shakeup satellites peak (indicated as “Sat.”) in Fig. 4c. The two characteristic peaks at 778.0 eV and 794.1 eV are assigned to Co<sup>0</sup>. The peaks at around 779.3 eV and 794.7 eV can be attributed to Co<sup>3+</sup>, while peaks around 781.2 eV and 796.9 eV are ascribed to Co<sup>2+</sup>. The Zn 2p spectrum (Fig. 4d) has two distinct peaks at 1021.8 eV and 1044.8 eV, corresponding to Zn 2p<sub>3/2</sub> and Zn 2p<sub>1/2</sub> of the Zn species, respectively, indicating the presence of Zn<sup>2+</sup>. As shown in Fig. 4e, the characteristic peaks in the full spectrum of Zn/Co-NPC700 correspond to C, N, Zn, and Co, respectively. The Raman spectra in Fig. 4f show that there are three distinct Raman peaks around 1360 cm<sup>-1</sup>, 1590 cm<sup>-1</sup>, and 2730 cm<sup>-1</sup>, which correspond to the D, G, and 2D bands, respectively. The band intensity ratios  $I_D/I_G$  of Zn/Co-NPC600, Zn/Co-NPC700, and Zn/Co-NPC800 are 0.94, 1.08, and 1.04, respectively. The high  $I_D/I_G$  band intensity ratio of Zn/Co-NPC700 indicates that defects are produced

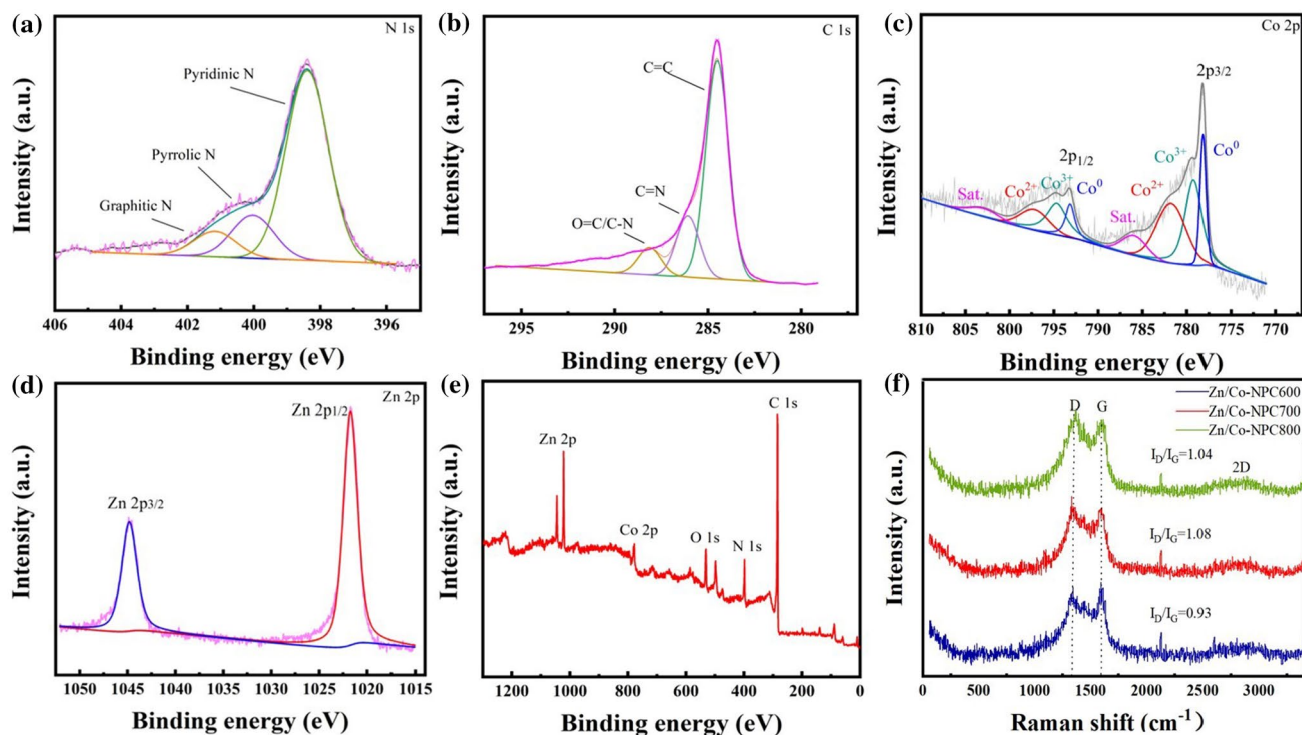


**Fig. 4** XPS spectrum of Zn/Co-NPC700 (a) N 1s; (b) C 1s; (c) Co 2p; (d) Zn 2p; (e) full spectrum; (f) Raman spectrum of Zn/Co-NPC composites.



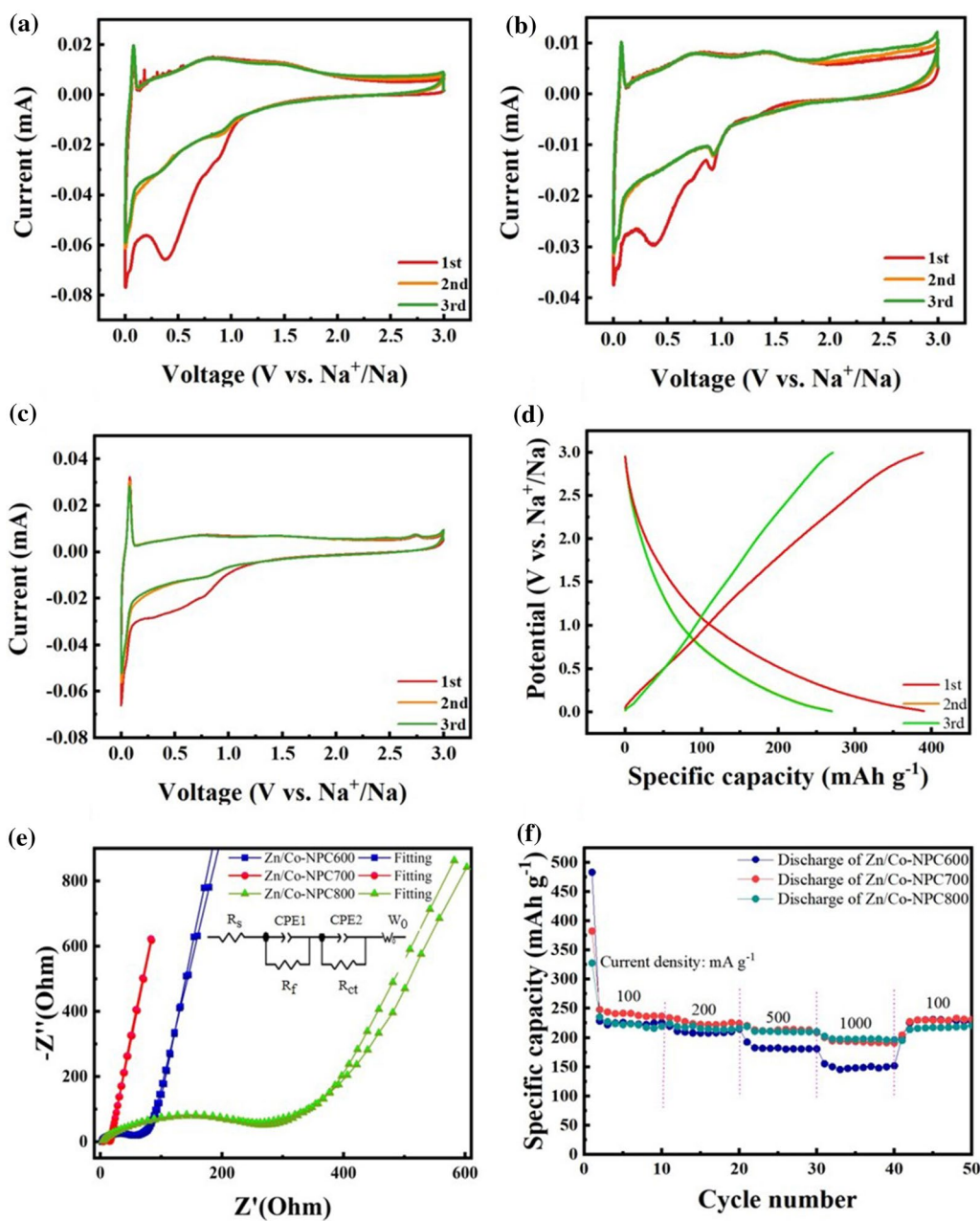


**Fig. 5** CV curves of (a) Zn/Co-NPC600, (b) Zn/Co-NPC700, and (c) Zn/Co-NPC800; (d) the charge–discharge curves of Zn/Co-NPC700 electrode material at the current density of  $100 \text{ mA g}^{-1}$ ; (e) Nyquist

spectra and its fitting lines of Zn/Co-NPC electrode materials and the equivalent circuit displayed in the inset; (f) rate cycling performance comparison of Zn/Co-NPC electrode materials.

to balance carbonization at the heat treatment temperature, which will provide more defects in long-term electrochemical cycling of a sodium-ion battery.<sup>25,26</sup>

### Electrochemical Performance of the Zn/Co-NPC Composites

The Zn/Co-NPC composites derived from Zn/Co-ZIF precursors at different temperatures are NPC materials

decorated with metallic elements. When used as anode materials for sodium-ion batteries, the special structure of Zn/Co-NPC composites make it have excellent electrochemical properties. Figure 5a, b, and c show the cyclic voltammetry (CV) curves of Zn/Co-NPC composites at a scan rate of  $0.1 \text{ mV s}^{-1}$  and a voltage range of 0.01–3.00 V. In the first cycle and subsequent cycles, a pair of sharp redox peaks appear near 0 V due to  $\text{Na}^+$  insertion and extraction in the Zn/Co-NPC electrode.<sup>27,28</sup> The Zn/Co-NPC800 electrode

material has a wide peak between 0.4 V and 1.0 V in the first cycle, which should be attributed to the formation of the solid electrolyte interface and the reaction between sodium ions and the electrode surface functional groups. The wide cathode peaks appear near 0.4 V and 1.1 V, due to the initial decomposition of electrolytes and other irreversible reactions forming the solid electrolyte interphase (SEI).<sup>29</sup> The peaks at about 1.0 V and 1.5 V are the conversion reaction of Zn and the extraction reaction of sodium ions, respectively.<sup>30</sup> In the CV curve of Zn/Co-NPC800, the peak decreases, which proves that a small amount of Zn evaporates with increasing temperature, which is consistent with the above structural characterization. The subsequent cyclic CV curves are almost identical, indicating that Zn/Co-NPC composites have high reversibility in the process of sodium insertion/extraction. The galvanostatic discharge/charge profiles of Zn/Co-NPC700 electrode material in the first three cycles with current density of 100 mA g<sup>-1</sup> are shown in Fig. 5d. The initial discharge and charge capacity of the Zn/Co-NPC700 electrode material are 389.9 and 278.9 mAh g<sup>-1</sup>, respectively, and the initial coulomb efficiency is 68.6%. This can be attributed to the formation of SEI films at the electrolyte interface, resulting in irreversible capacity, which matches well with the above CV curves.

Figure 5e shows Nyquist spectra (frequency range: 0.01–100 kHz) of the alternating current impedance of the Zn/Co-NPC composites, which can be well fit to the equivalent circuit diagram in the illustration. The low-frequency region and high-frequency region in the Nyquist spectra are shown as a straight line and a semicircle, respectively. It is mainly composed of charge transfer resistance (R<sub>ct</sub>), component solution resistance (R<sub>s</sub>, R<sub>f</sub>), double layer capacitance (CPE1, CPE2) and diffusion impedance (W<sub>0</sub>).<sup>31–33</sup> The R<sub>ct</sub> values of the Zn/Co-NPC600, Zn/Co-NPC700, and Zn/

Co-NPC800 composites are 27.84 Ω, 5.38 Ω, and 184.3 Ω, respectively. The Zn/Co-NPC700 electrode material has better electronic properties due to its lower resistance.<sup>34</sup> The R<sub>ct</sub> value of the Zn/Co-NPC800 composite is high, indicating that the conductivity and reaction rate of the material are low.<sup>35</sup> This shows that Zn/Co-NPC700 electrode material has high conductivity when used as electrode material for sodium-ion batteries, which is beneficial for the insertion/extraction of sodium ions.<sup>36</sup>

Figure 5f presents the rate properties of three groups of Zn/Co-NPC electrode materials at current densities of 100 mA g<sup>-1</sup>, 200 mA g<sup>-1</sup>, 500 mA g<sup>-1</sup>, 1000 mA g<sup>-1</sup>, and 100 mA g<sup>-1</sup>, respectively. The discharge specific capacity of the Zn/Co-NPC electrode materials decays at the initial stage, which can be attributed to the irreversible capacity loss caused by the formation of SEI film. The average discharge specific capacity values of the Zn/Co-NPC700 electrode material are 254.8 mAh g<sup>-1</sup>, 225.9 mAh g<sup>-1</sup>, 213.5 mAh g<sup>-1</sup>, and 193.6 mAh g<sup>-1</sup> at various current densities ranging from 100 mA g<sup>-1</sup> to 1000 mA g<sup>-1</sup>, respectively. When the current density returns to 100 mA g<sup>-1</sup>, the discharge specific capacity of the Zn/Co-NPC700 electrode material is up to 227.8 mAh g<sup>-1</sup>. Compared with the other two groups of samples, the Zn/Co-NPC700 electrode material has higher discharge capacity and better rate capability. This is mainly because the suitable pore structure of the Zn/Co-NPC700 electrode material provides a suitable transport space for sodium ions, and facilitates rapid transfer of sodium ions/electrons.<sup>11,37</sup> For the porous carbon structure, Zn/Co-NPC electrode materials can effectively alleviate the damage to electrode materials in the process of sodium-ion embedding/unembedding.<sup>38</sup> Therefore, when used as anode material for sodium-ion batteries, Zn/Co-NPC composites have suitable porous structure and specific surface area. This

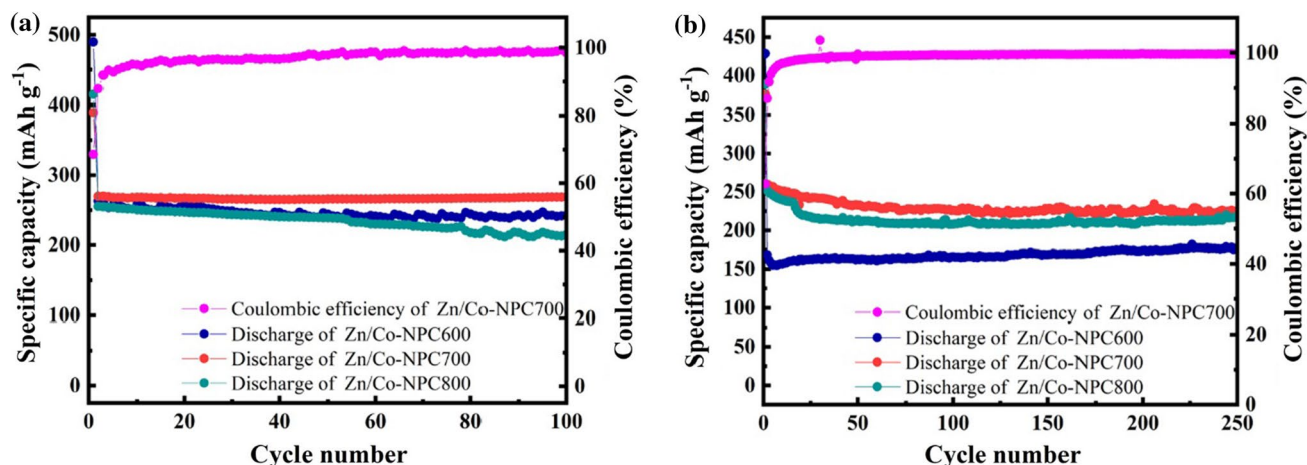


**Fig. 6** Cycling performance of Zn/Co-NPC electrode materials at (a) current density of 100 mA g<sup>-1</sup> for 100 cycles; (b) current density of 500 mA g<sup>-1</sup> for 250 cycles.



helps to provide more active sites and diffusion pathways, thereby obtaining excellent electrochemical performance.

The cycling performance curves of three groups of Zn/Co-NPC electrode materials at a current density of  $100 \text{ mA g}^{-1}$  are shown in Fig. 6a. The first discharge specific capacity values of Zn/Co-NPC600, Zn/Co-NPC700, and Zn/Co-NPC800 are  $489.6 \text{ mAh g}^{-1}$ ,  $380.9 \text{ mAh g}^{-1}$ , and  $415 \text{ mAh g}^{-1}$ , respectively. Zn/Co-NPC600 has a high specific capacity for the first discharge, but it decays more severely in subsequent cycles. This is mainly due to the large specific surface area, which causes a violent and irreversible reaction between sodium and the surface.<sup>39</sup> The Zn/Co-NPC800 electrode material drops to  $240.5 \text{ mAh g}^{-1}$  after 100 cycles. However, the Zn/Co-NPC700 electrode material remains at  $269.1 \text{ mAh g}^{-1}$  after 100 cycles. The results show that Zn/Co-NPC700 electrode material has higher specific capacity and good cycle stability compared with the other two groups.

Figure 6b shows the cycling performance of the three groups of Zn/Co-NPC electrode materials for 250 cycles at a current density of  $500 \text{ mA g}^{-1}$ . As can be seen from Fig. 6b, the first discharge specific capacity values of Zn/Co-NPC600, Zn/Co-NPC700, and Zn/Co-NPC800 electrode materials are  $428.0 \text{ mAh g}^{-1}$ ,  $376.3 \text{ mAh g}^{-1}$ , and  $388.9 \text{ mAh g}^{-1}$ , respectively. However, in the late cycle, the values are  $191.2 \text{ mAh g}^{-1}$ ,  $224.6 \text{ mAh g}^{-1}$ , and  $217.6 \text{ mAh g}^{-1}$  after 250 cycles, respectively. Obviously, Zn/Co-NPC700 electrode material still has good cycle stability even at high current density. The results show that Zn/Co-NPC700 electrode material becomes reversible and stable anode material for sodium-ion batteries due to its excellent cycle stability and rate performance. This is attributed to the rich pore structure, high specific surface area, and good electrical conductivity of the Zn/Co-NPC composite.

Combined with the relationship between structure and performance, Zn/Co-NPC700 electrode materials have

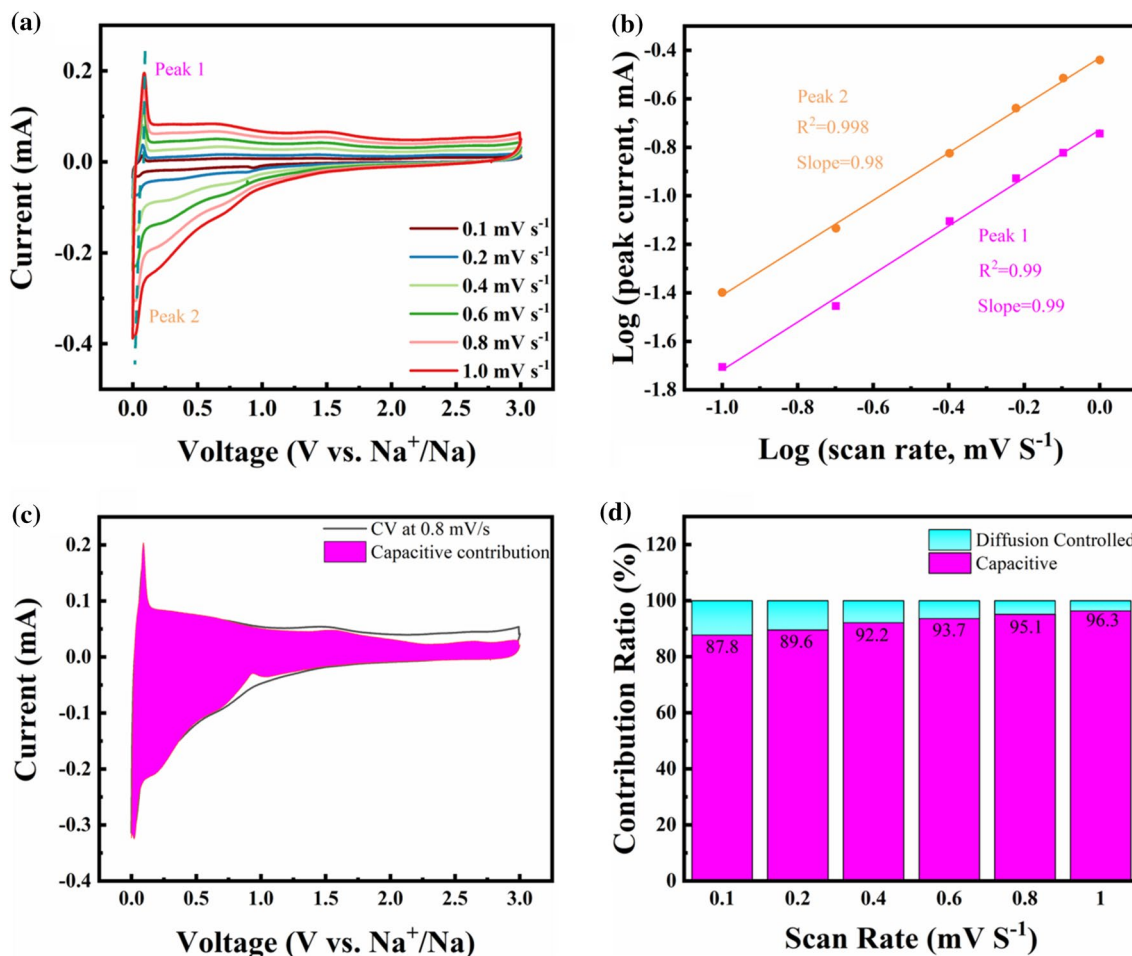


**Fig. 7** (a) CV curves of Zn/Co-NPC700 electrode material at varied scan rates from  $0.1 \text{ mV s}^{-1}$  to  $1.0 \text{ mV s}^{-1}$ ; (b) the functional relationship between current and scanning rate for peak 1 and peak 2; (c)

capacitive contribution and diffusion contribution of Zn/Co-NPC700 electrode material at  $0.8 \text{ mV s}^{-1}$ ; (d) the contribution ratio of Zn/Co-NPC electrode materials.

excellent electrochemical performance for the following reasons: (1) Compared with the other two groups of electrode materials, Zn/Co-NPC700 has a suitable porous structure, which helps to shorten the transport path of electrons and sodium ions, thereby improving sodium-ion storage. (2) For the polyhedral frame of Zn/Co-NPC composites, Zn/Co-NPC electrode materials can effectively alleviate the damage to electrode materials in the process of sodium insertion/extraction.

The electrochemical kinetic mechanism of this composite is evaluated by measuring the CV curves of the Zn/Co-NPC700 composite at different scanning rates (0.1–1.0 mV s<sup>-1</sup>). As shown in Fig. 7a, with the increase in scanning rate, the shape of the CV curves has no obvious change, which indicates that the Zn/Co-NPC700 electrode material has excellent rate performance. The functional relationship between current and scanning rate<sup>35</sup> is shown in Eq. 3, where a and b are constants, and b is determined by the slope of the line segment in Eq. 4. When the value of b is close to 0.5, it represents ion diffusion control behavior; when the b value is close to 1.0, it represents capacitance behavior.<sup>40,41</sup> It can be seen from Fig. 7b that the calculated b values of the potential for the two selected redox peaks are 0.99 and 0.98, respectively. The results show that the diffusion control of sodium ions in Zn/Co-NPC700 electrode material is mainly determined by the capacitance behavior.

$$i = av^b \quad (3)$$

$$\log i = b \times \log v + \log a \quad (4)$$

$$i = k_1v + k_2v^{1/2} \quad (5)$$

The contribution percentage of the pseudocapacitive behavior is calculated by Eq. 5. As shown in Fig. 7c, the capacitance contribution of Zn/Co-NPC700 electrode material is about 95.1% at 0.8 mV s<sup>-1</sup>. The contribution ratio at other scanning rates is also calculated as shown in Fig. 7d. The results show that as the scanning speed increases, the contribution rate of capacitive control increases as well. When the scanning rate increases to 1.0 mV s<sup>-1</sup>, the contribution percentage rises to 96.3%. The results show that the capacitive behavior plays an important role with the increase in scanning rate.

## Conclusion

In summary, NPC composites were simply synthesized by heat treatment of Zn/Co-ZIFs in a N<sub>2</sub> atmosphere. Zn/Co-NPC700 electrode material demonstrated high specific

capacity, excellent long-term cycle stability, and superior rate performance when used as anode materials for sodium-ion batteries. Its excellent electrochemical performance is due to the special porous structure and high specific surface area of the Zn/Co-NPC composite, which provides a smoother channel for the transfer of sodium ions. The NPC also improves the conductivity of the material. Taken together, the results show that the composite materials obtained by heat treatment of Zn/Co-ZIFs at different temperatures have the advantage of a special structure and adjustable pore size. Additional research can further explore the influence of these features on the electrochemical properties, as well as their repeatability and scalability.

**Supplementary Information** The online version contains supplementary material available at <https://doi.org/10.1007/s11664-024-10935-y>.

**Acknowledgments** The authors would like to acknowledge North China University of Science and Technology.

**Author Contributions** CS: experimental operation, designed the experimental plan, drawing, text editing and writing. XL: organized data and plot, collected literature information. JW: organized data and plot, collected literature information. SY: designed the experimental plan and checked the manuscript.

**Data Availability** The datasets generated during and/or analyzed during the current study are available from the corresponding author on reasonable request.

**Conflict of interest** The authors declare that they have no conflict of interest.

## References

1. P.K. Nayak, L.T. Yang, W. Brehm, and P. Adelhelm, From lithium-ion to sodium-ion batteries: advantages, challenges, and surprises. *Angew. Chem. Int. Ed.* 57, 102 (2018).
2. P. Yadav, A. Patrike, K. Wasnik, V. Shelke, and M. Shelke, Strategies and practical approaches for stable and high energy density sodium-ion battery: a step closer to commercialization. *Mater. Today Sustain.* 23, 100385 (2022).
3. V. Palomares, P. Serras, I. Villaluenga, K.B. Hueso, J. Carretero-Gonzalez, and T. Rojo, Na-ion batteries, recent advances and present challenges to become low cost energy storage systems. *Energy Environ. Sci.* 5, 5884 (2012).
4. Q.D. Wang, C.L. Zhao, Y.X. Lu, Y.M. Li, Y.H. Zheng, Y.R. Qi, X.H. Rong, L.W. Jiang, X. Qi, Y.J. Shao, D. Pan, B.H. Li, Y.S. Hu, and L.Q. Chen, Advanced nanostructured anode materials for sodium-ion batteries. *Small* 13, 1701835 (2017).
5. E. Gabriel, C.R. Ma, K. Graff, A. Conrado, D.W. Hou, and H. Xiong, Heterostructure engineering in electrode materials for sodium ion batteries: recent progress and perspectives. *eScience* 3, 100139 (2023).
6. M.M. Doeff, Y.P. Ma, S.J. Visco, and L.C. De Jonghe, Electrochemical insertion of sodium into carbon. *J. Electrochem. Soc.* 140, L169 (1993).
7. D. Alvira, D. Antoran, and J.J. Manya, Plant-derived hard carbon as anode for sodium-ion batteries: a comprehensive review to guide interdisciplinary research. *Chem. Eng. J.* 447, 137468 (2022).

8. Y.L. Miao, J. Zong, and X.J. Liu, Phosphorus-doped pitch-derived soft carbon as an anode material for sodium ion batteries. *Mater. Lett.* 188, 355 (2017).
9. K. Anish Raj, M.R. Panda, D.P. Dutta, and S. Mitra, Bio-derived mesoporous disordered carbon: an excellent anode in sodium-ion battery and full-cell lab prototype. *Carbon* 143, 402 (2019).
10. F.F. Lei, Y.Q. Cao, R.W. Wang, Z.T. Zhang, and S.L. Qiu, Ultra-long cycle life and high rate sodium-ion batteries enabled by surface-dominated storage of 3D hollow carbon spheres. *J. Alloys Compd.* 926, 166646 (2022).
11. J. Wen, Z.W. Ding, X.P. Wang, R. Jiang, L. Ma, L.L. Guan, Y. Ren, Z. Liu, X. Chen, and X.W. Zhou, Molecular self-assembly derived hollow mesoporous carbon nanospheres with different pore and wall structure as ultra-stable anode for sodium-ion batteries. *Electrochim. Acta* 430, 141080 (2022).
12. H. Gong, T. Du, L.Y. Liu, L.F. Zhou, Y.S. Wang, H. Jia, and Z.Y. Cheng, Self-source silicon embedded in 2D biomass-based carbon sheet as anode material for sodium ion battery. *Appl. Surf. Sci.* 586, 152759 (2022).
13. A. Agrawal, S. Janakiraman, K. Biswas, A. Venimadhav, S. Srivastava, and S. Ghosh, Understanding the improved electrochemical performance of nitrogen-doped hard carbons as an anode for sodium ion battery. *Electrochim. Acta* 317, 164 (2019).
14. F.Y. Xiao, W. Gao, H. Wang, Q. Wang, S.J. Bao, and M.W. Xu, A new calcium metal organic frameworks (Ca-MOF) for sodium-ion batteries. *Mater. Lett.* 286, 129264 (2021).
15. Y.J. Xu, D.X. Wang, G.L. Luo, and Y.L. Xiang, First-principles study of ZIF-8 as anode for Na and K ion batteries. *Colloids Surf A Physicochem Eng Asp* 659, 130802 (2023).
16. Y. Zheng, X.P. Ni, K.M. Li, X.H. Yu, H. Song, S. Chen, N. Khan, D. Wang, and C. Zhang, Multi-heteroatom-doped hollow carbon nanocages from ZIF-8@CTP nanocomposites as high-performance anodes for sodium-ion batteries. *Compos. Commun.* 32, 101116 (2022).
17. Y.V. Kaneti, J. Zhang, Y.B. He, Z.J. Wang, S. Tanaka, M.A. Hossein, Z.Z. Pan, B. Xiang, Q.H. Yang, and Y. Yamauchi, Fabrication of an MOF-derived heteroatom-doped Co/CoO/carbon hybrid with superior sodium storage performance for sodium-ion batteries. *J. Mater. Chem. A* 5, 15356 (2017).
18. H.R. Xu, L.L. Zhao, X.M. Liu, Q.S. Huang, Y.Q. Wang, C.X. Hou, Y.Y. Hou, J. Wang, F. Dang, and J.T. Zhang, Metal-organic-framework derived core-shell N-doped carbon nanocages embedded with cobalt nanoparticles as high-performance anode materials for lithium-ion batteries. *Adv. Funct. Mater.* 30, 2006188 (2020).
19. Z. Yu, Y. Bai, S.M. Zhang, Y.X. Liu, N.Q. Zhang, G.H. Wang, J.H. Wei, Q.B. Wu, and K.N. Sun, Metal-organic framework derived Co<sub>3</sub>ZnC/Co embedded in nitrogen doped CNT-grafted carbon polyhedra as high-performance electrocatalyst for water splitting. *ACS Appl. Mater. Inter.* 10, 6245 (2018).
20. Y.L. Zhu, Y.X. Wang, C. Gao, W.N. Zhao, X.B. Wang, and M.B. Wu, CoMoO<sub>4</sub>-N-doped carbon hybrid nanoparticles loaded on a petroleum asphalt-based porous carbon for lithium storage. *New Carbon Mater.* 35, 358 (2020).
21. R.M. Huang, D. Liao, Z.H. Liu, J.G. Yu, and X.Y. Jiang, Electrostatically assembling 2D hierarchical Nb<sub>2</sub>CTx and ZIFs-derivatives into Zn-Co-NC nanocage for the electrochemical detection of 4-nitrophenol. *Sens. Actuator B Chem.* 338, 129828 (2021).
22. Q.Q. Chen, H. Jiang, and R.Z. Chen, Synthesis of ZIF-67 derived Co-based catalytic membrane for highly efficient reduction of p-nitrophenol. *Chem End Sci.* 248, 117160 (2022).
23. Z.Y. Qu, M.H. Zhou, J.X. Zhang, H. Jiang, and R.Z. Chen, ZIF-derived Co@carbon nanofibers for enhanced chemical fixation of CO<sub>2</sub>. *Sep. Purif. Technol.* 310, 123196 (2023).
24. X.D. Shi, Z. Zhang, Y. Fu, and Y.Q. Gan, Self-template synthesis of nitrogen-doped porous carbon derived from zeolitic imidazolate framework-8 as an anode for sodium-ion batteries. *Mater. Lett.* 161, 332 (2015).
25. S.F. Tan, M.L. Fan, W.M. Tu, D.X. Zhang, Q. Li, Z.Y. Xu, X.Y. Yang, H.F. Pan, and H.N. Zhang, Crystalline-amorphous Co/Co<sub>3</sub>O<sub>4</sub> derived from a low-temperature etching of ZIF-67 for oxygen-involved catalytic reactions. *Appl. Surf. Sci.* 640, 158266 (2023).
26. J.W. Su, G.L. Xia, R. Li, Y. Yang, J.T. Chen, R.H. Shi, P. Jiang, and Q.W. Chen, Co<sub>3</sub>ZnC/Co nano-heterojunctions encapsulated in nitrogen-doped graphene layers derived from PBAs as highly efficient bi-functional electrocatalysts for both OER and ORR. *J. Mater. Chem. A* 4, 9212 (2016).
27. D. Qin, Z.Y. Liu, Y.Z. Zhao, G.Y. Xu, F. Zhang, and X.G. Zhang, A sustainable route from corn stalks to N, P-dual doping carbon sheets toward high performance sodium-ion batteries anode. *Carbon* 130, 664 (2018).
28. L.Y. Suo, J.H. Zhu, X.Y. Shen, Y.Z. Wang, X. Han, Z.Q. Chen, Y. Li, Y.R. Liu, D. Wang, and Y.W. Ma, Hard carbon spheres interconnected by carbon nanotubes as high-performance anodes for sodium-ion batteries. *Carbon* 151, 1 (2019).
29. H.J. Wang, J.L. Lan, H.C. Yuan, S.C. Luo, Y.Q. Huang, Y.H. Yu, Q. Cai, and X.P. Yang, Chemical grafting-derived N, P Co-doped hollow microporous carbon spheres for high-performance sodium-ion battery anodes. *Appl. Surf. Sci.* 518, 146221 (2020).
30. R.P. Zhang, J.J. Xu, M. Jia, E.Z. Pan, C.L. Zhou, and M.Q. Jia, Ultrafine ZnS quantum dots decorated reduced graphene oxide composites derived from ZIF-8/graphene oxide hybrids as anode for sodium-ion batteries. *J. Alloys Compd.* 781, 450 (2019).
31. Y.Y. He, L. Wang, C.F. Dong, C.C. Li, X.Y. Ding, Y.T. Qian, and L.Q. Xu, In-situ rooting ZnSe/N-doped hollow carbon architectures as high-rate and long-life anode materials for half/full sodium-ion and potassium-ion batteries. *Energy Storage Mater.* 23, 35 (2019).
32. H.M. Li, T.L. Wang, X. Wang, G.D. Li, J.X. Shen, and J.L. Chai, MOF-derived Al-doped Na<sub>2</sub>FePO<sub>4</sub>F/mesoporous carbon nanonetwork composites as high-performance cathode material for sodium-ion batteries. *Electrochim. Acta* 373, 137905 (2021).
33. Z.P. Xu, Y. Huang, C. Chen, L. Ding, Y.D. Zhu, Z. Zhang, and Z.X. Guang, MOF-derived hollow Co(Ni)Se<sub>2</sub>/N-doped carbon composite material for preparation of sodium ion battery anode. *Ceram. Int.* 46, 4532 (2020).
34. H.X. Chen, Y.T. Yang, R.H. Nie, C. Li, S.W. Xu, M.C. Zhou, X.Y. Zhang, and H.M. Zhou, Micro-nano Na<sub>3</sub>V<sub>2</sub>(PO<sub>4</sub>)<sub>3</sub>/C derived from metal-organic frameworks for high performance sodium ion batteries. *J. Alloys Compd.* 932, 167695 (2023).
35. L.K. Fu, C.X. Kang, W.Q. Xiong, P.F. Tian, S.Y. Cao, S.Y. Wan, H.Y. Chen, C.B. Zhou, and Q.M. Liu, WS<sub>2</sub> nanosheets@ZIF-67-derived N-doped carbon composite as sodium ion battery anode with superior rate capability. *J. Colloid Interface Sci.* 595, 59 (2021).
36. J.B. Li, D. Yan, S.J. Hou, T. Lu, Y.F. Yao, and L.K. Pan, Metal-organic frameworks converted flower-like hybrid with Co<sub>3</sub>O<sub>4</sub> nanoparticles decorated on nitrogen-doped carbon sheets for boosted lithium storage performance. *Chem. Eng. J.* 354, 172 (2018).
37. Z.Y. Huang, Y.F. Yuan, Z.J. Yao, M. Zhu, S.M. Yin, Y.Z. Huang, S.Y. Guo, and W.W. Yan, Metal-organic framework-derived ultrafine CoSe nanocrystal@honeycomb porous carbon nanofiber as multidimensional advanced anode for sodium-ion batteries. *Appl. Surf. Sci.* 637, 157886 (2023).
38. G.Q. Zou, X.N. Jia, Z.D. Huang, S.M. Li, H.X. Liao, H.S. Hou, L.P. Huang, and X.B. Ji, Cube-shaped porous carbon derived from MOF-5 as advanced material for sodium-ion batteries. *Electrochim. Acta* 96, 413 (2016).
39. Y.M. Hu, Y.P. Chen, Y. Liu, W.X. Li, M.Y. Zhu, P.F. Hu, H.M. Jin, and Y. Li, Accordion-like nanoporous carbon derived from Al-MOF as advanced anode material for sodium-ion batteries. *Microporous Mesoporous Mat.* 270, 67 (2018).
40. W.L. Feng, V.S. Avvaru, S.J. Hinder, and V. Etacheri, High-energy sodium-ion hybrid capacitors through nanograin-boundary-induced

- pseudocapacitance of  $\text{Co}_3\text{O}_4$  nanorods. *J. Energy Chem.* 69, 338 (2022).
41. J.J. Liu, J.L. Li, S.M. Guo, S.W. Yao, J.M. Liu, F.X. Cheng, and S.B. Xia, Porous CoP@RGO with pseudocapacitance characteristics for lithium ion storage. *Scripta Mater.* 201, 113983 (2021).

Springer Nature or its licensor (e.g. a society or other partner) holds exclusive rights to this article under a publishing agreement with the author(s) or other rightsholder(s); author self-archiving of the accepted manuscript version of this article is solely governed by the terms of such publishing agreement and applicable law.

**Publisher's Note** Springer Nature remains neutral with regard to jurisdictional claims in published maps and institutional affiliations.